

LETTER TO THE EDITOR

# The atomic gas of star-forming galaxies at $z \sim 0.05$ as revealed by the Five-hundred-meter Aperture Spherical Radio Telescope

Cheng Cheng<sup>1,2,3</sup>, Edo Ibar<sup>4</sup>, Wei Du<sup>2,3</sup>, Juan Molina<sup>5,6,7</sup>, Gustavo Orellana-González<sup>8,9</sup>, Bo Zhang<sup>2</sup>, Ming Zhu<sup>2</sup>, Cong Kevin Xu<sup>1,2,3</sup>, Shumei Wu<sup>1,2,3</sup>, Tianwen Cao<sup>1,2,3</sup>, Jia-Sheng Huang<sup>1,2,3</sup>, Roger Leiton<sup>9</sup>, Thomas M. Hughes<sup>1,4,10,11</sup>, Chuan He<sup>1,2,3</sup>, Zijian Li<sup>1,2,3</sup>, Hai Xu<sup>1,2,3</sup>, Y. Sophia Dai<sup>1,2,3</sup>, Xu Shao<sup>1,2,3</sup>, Marat Musin<sup>1,2,3</sup>

<sup>1</sup> Chinese Academy of Sciences South America Center for Astronomy, National Astronomical Observatories, CAS, Beijing 100101, China.

e-mail: chengcheng@nao.cas.cn

<sup>2</sup> National Astronomical Observatories, Chinese Academy of Sciences (NAOC), 20A Datun Road, Chaoyang District, Beijing 100101, China

<sup>3</sup> CAS Key Laboratory of Optical Astronomy, National Astronomical Observatories, Chinese Academy of Sciences, Beijing 100101, China

<sup>4</sup> Instituto de Física y Astronomía, Universidad de Valparaíso, Avda. Gran Bretaña 1111, Valparaíso, Chile.

<sup>5</sup> Kavli Institute for Astronomy and Astrophysics, Peking University, 5 Yiheyuan Road, Haidian District, Beijing 100871, P.R. China

<sup>6</sup> Department of Astronomy, School of Physics, Peking University, Beijing 100871, China

<sup>7</sup> Departamento de Astronomía (DAS), Universidad de Chile, Casilla 36-D, Santiago, Chile

<sup>8</sup> Departamento de Matemática y Física Aplicadas, Universidad Católica de la Santísima Concepción, Alonso de Ribera 2850, Concepción, Chile

<sup>9</sup> Departamento de Astronomía, Universidad de Concepción, Casilla 160-C, Concepción, Chile

<sup>10</sup> CAS Key Laboratory for Research in Galaxies and Cosmology, Department of Astronomy, University of Science and Technology of China, Hefei 230026, China

<sup>11</sup> School of Astronomy and Space Science, University of Science and Technology of China, Hefei 230026, China

June 11, 2020

## ABSTRACT

**Context.** We report new H I observations of four  $z \sim 0.05$  VALES galaxies undertaken during the commissioning phase of the Five-hundred-meter Aperture Spherical Radio Telescope (FAST).

**Aims.** FAST is the largest single-dish telescope in the world, with a 500 meter aperture and a 19-Beam receiver. Exploiting the unprecedented sensitivity provided by FAST, we aim to study the atomic gas content, via the H I 21 cm emission line, in low- $z$  star formation galaxies taken from the Valparaíso ALMA/APEX Line Emission Survey (VALES). Together with previous Atacama Large Millimeter/submillimeter Array (ALMA) CO( $J = 1 - 0$ ) observations, the H I data provides crucial information to measure the gas mass and dynamics.

**Methods.** As a pilot H I galaxy survey, we targeted four local star-forming galaxies at  $z \sim 0.05$ . In particular, one of them has already been detected in H I by the Arecibo Legacy Fast ALFA survey (ALFALFA), allowing a careful comparison. We use an ON-OFF observing approach that allowed us to reach an rms of  $0.7 \text{ mJy beam}^{-1}$  at a  $1.7 \text{ km s}^{-1}$  velocity resolution within only 20 minutes ON-target integration time.

**Results.** In this letter, we demonstrate the great capabilities of the FAST 19-beam receiver for pushing the detectability of the H I emission line of extra-galactic sources. The H I emission line detected by FAST shows good consistency with the previous Arecibo telescope ALFALFA results. Our observations are put in context with previous multi-wavelength data to reveal the physical properties of these low- $z$  galaxies. We find that the CO( $J = 1 - 0$ ) and H I emission line profiles are similar. The dynamical mass estimated from the H I data is an order of magnitude higher than the baryon mass and the dynamical mass derived from the CO observations, implying that the mass probed by dynamics of H I is dominated by the dark matter halo. In one case, a target shows an excess of CO( $J = 1 - 0$ ) in the line centre, which can be explained by an enhanced CO( $J = 1 - 0$ ) emission induced by a nuclear starburst showing high velocity dispersion.

**Key words.** Galaxies: evolution – Galaxies: ISM – Galaxies: star formation – Galaxies: starburst – Radio lines: galaxies

## 1. Introduction

Atomic neutral hydrogen gas, H I, is found to be one of the most extended baryon components of galaxies (Yun et al. 1994). The width of the H I emission line has been historically used to estimate the dynamical mass via the large-scale rotation velocity derived from the double horn shape of the emission line (Roberts 1978). These estimates provide a proxy for estimat-

ing the dark matter content in galaxies (Salucci 2019). On the other hand, the optically thin nature of the H I emission leads to the possibility of probing possible gas inflows via the asymmetry of the line profile (Bournaud et al. 2005; Deg et al. 2020). The H I fluxes are found to follow very well scaling relations such as: the star formation rate (SFR) surface density  $\Sigma_{\text{SFR}}$  and the combined surface density of molecular ( $\text{H}_2$ ) and H I gas,  $\Sigma_{\text{HI}+\text{H}_2}$  (Schmidt 1959; Kennicutt 1998), H I mass vs. stellar mass

(Huang et al. 2012; Maddox et al. 2015), H $\alpha$  mass vs. H $\alpha$  size (Wang et al. 2016; Stevens et al. 2019) and the H $\alpha$ -to-H $\beta$  ratio as a function of stellar or gas surface density (Leroy et al. 2008). These relations enable us to the revelation of important information even when we are unable to perform spatially resolved H $\alpha$  observations (Giovanelli & Haynes 2015).

Given the fundamental importance of the H $\alpha$  component, several wide-field H $\alpha$  surveys have been carried out to probe the neutral atomic gas at low redshift. Previous blind H $\alpha$  surveys such as the H $\alpha$  Parkes All-Sky Survey (HIPASS, Barnes et al. 2001; Meyer et al. 2004; Wong et al. 2006, 13 beams), the H $\alpha$  Jodrell All Sky Survey (Lang et al. 2003, 4 beams), the Effelsberg-Bonn H $\alpha$  Survey (EBHIS, Winkel et al. 2010; Kerp et al. 2011, 7 beams), and the Arecibo Legacy Fast ALFA Survey (ALFALFA, Giovanelli et al. 2005, 7 beams) have detected large numbers of gas rich galaxies in both northern and southern skies. The ongoing Widefield ASKAP L-band Legacy All-sky Blind survey (WALLABY, Koribalski et al. 2020), and Deep Investigation of Neutral Gas Origins (DINGO, Meyer 2009) are planning to perform an H $\alpha$  survey over much larger areas using the Australian Square Kilometer Array Pathfinder (ASKAP), expecting to detect a million new H $\alpha$  sources up to  $z \sim 0.4$ .

Current facilities have been able to detect the H $\alpha$  emission line up to  $z = 0.1$  (e.g., Giovanelli & Haynes 2015). Major factors limiting the detectability of higher redshift sources include the sensitivity, the detector frequency range and Radio Frequency Interference (RFI). One way to overcome the sensitivity issues is by using gravitational magnification. For example, H $\alpha$  ultra-deep survey projects such as Blind Ultra Deep H $\alpha$  Environmental Survey (BUDHIES Jaffé et al. 2013), or the COSMOS H $\alpha$  Large Extragalactic Survey (CHILES) have spend hundreds of hours to extend the H $\alpha$  detection up to  $z \approx 0.3$  ( $z = 0.37$  in Fernández et al. 2016, and  $z = 0.32$  in Rhee et al. 2018). Higher redshift H $\alpha$  studies have been available from damped Ly $\alpha$  absorbers (Neeleman et al. 2016), or intensity mapping (e.g., Hu et al. 2020). To detect the H $\alpha$  emission line beyond  $z \sim 0.1$  is still a major challenge.

The new fully operational Five-hundred-meter Aperture Spherical radio Telescope (FAST, Nan 2006; Nan et al. 2011) with the tracking active reflector design (Qiu 1998) can provide us the opportunity to probe H $\alpha$  in the higher redshift Universe with unprecedented sensitivity. For example, the upcoming Commensal Radio Astronomy FasT Survey (CRAFTS) project is expected to detect H $\alpha$  out to  $z = 0.35$  (Zhang et al. 2019). As the largest filled-aperture radio telescope, FAST has been designed to achieve many challenging scientific goals, including hunting for pulsar, H $\alpha$  map of local galaxies, mapping the Milky Way central region, etc (see the review of Jiang et al. 2019, 2020, and references therein).

In this letter, we report the results of our pilot H $\alpha$  survey with FAST on a sample of four  $z \sim 0.05$  star star-forming galaxies taken from the Valparaíso ALMA/APEX Line Emission Survey (Villanueva et al. 2017; Cheng et al. 2018). They are among of the first extragalactic H $\alpha$  detection cases observed by FAST in its commissioning phase. Throughout this paper, we assume a standard  $\Lambda$ CDM cosmology with  $H_0 = 70 \text{ km s}^{-1} \text{ Mpc}^{-1}$ ,  $\Omega_M = 0.3$ , and  $\Omega_\Lambda = 0.7$ . All magnitudes are provided in the AB magnitude system (Oke & Gunn 1983).

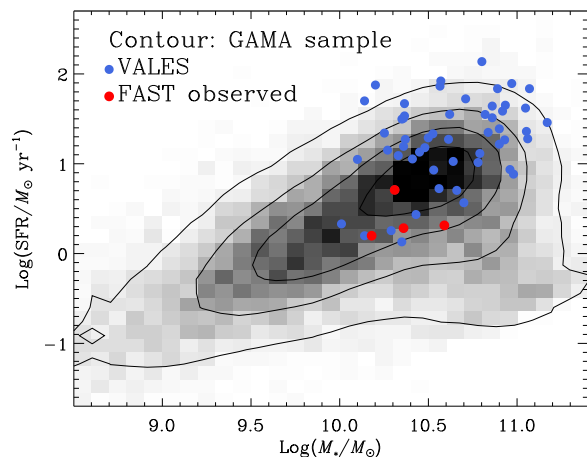


**Fig. 1.** Main sequence of the low- $z$  galaxies (black contour and grayscale) and our ALMA detected VALES sample (blue dots). The FAST observed targets are shown as red dots.

## 2. FAST observations

### 2.1. Sample selection

The ongoing VALES project has targeted the low- $J$  CO transitions in 91 low- $z$  dusty star-forming galaxies taken from the *Herschel* Astrophysical Terahertz Large Area Survey (*H-ATLAS*, Eales et al. 2010). The CO( $J = 1 - 0$ ) and CO( $J = 2 - 1$ ) emission lines have been observed using the Atacama Large Millimeter/sub-millimeter Array (ALMA, Villanueva et al. 2017) and the Atacama Pathfinder EXperiment (APEX, Cheng et al. 2018), respectively. The VALES galaxies are selected from the equatorial GAMA fields, which provides extensive multi-wavelength coverage (Driver et al. 2009).

In this pilot work, we extract four galaxies previously detected in CO( $J = 1 - 0$ ) to target their H $\alpha$  emission line with FAST. To mitigate sensitivity effects, we focus on those at the lower redshift end of the VALES distribution. This is particularly useful to avoid the strong RFI seen at lower frequencies. The targeted sources have: (1) an expected H $\alpha$  flux higher than  $0.5 \text{ Jy km s}^{-1}$  as estimated using the Zhang et al. (2009) prescription, (2) they do not have bright nearby galaxies at similar redshift within one beam (2.9 arcmin diameter), (3) their Declinations are in the range of 0 to 40 deg, so that we can have a high collecting area (full 300m dish). Most of the VALES galaxies are massive star forming galaxies as shown in Fig. 1. The observed four galaxies observed by FAST, shown as red dots, are local main sequence galaxies.

Aided by the previous coverage provided by ALFALFA (Haynes et al. 2011, 2018) in part of the GAMA fields, we include one source with ALFALFA measurements (HATLASJ083601.5+002617) to check consistency and the relative performance of the FAST telescope.

### 2.2. Observation setup and calibration

We were allocated 10 hours in L-band with the 19-Beam receiver during the FAST Commissioning Phase (Shared-risk Observing Proposal<sup>1</sup> 2019A-012-S; PI: Cheng Cheng). The focal plane is covered by 19 beams, each one with a 2.9 arcmin diameter and separated by 5.8 arcmin from each other. Our observations were carried out in the tracking mode, utilizing only the central beam

<sup>1</sup> [http://english.nao.cas.cn/ne2015/News2015/201902/t20190222\\_2](http://english.nao.cas.cn/ne2015/News2015/201902/t20190222_2)

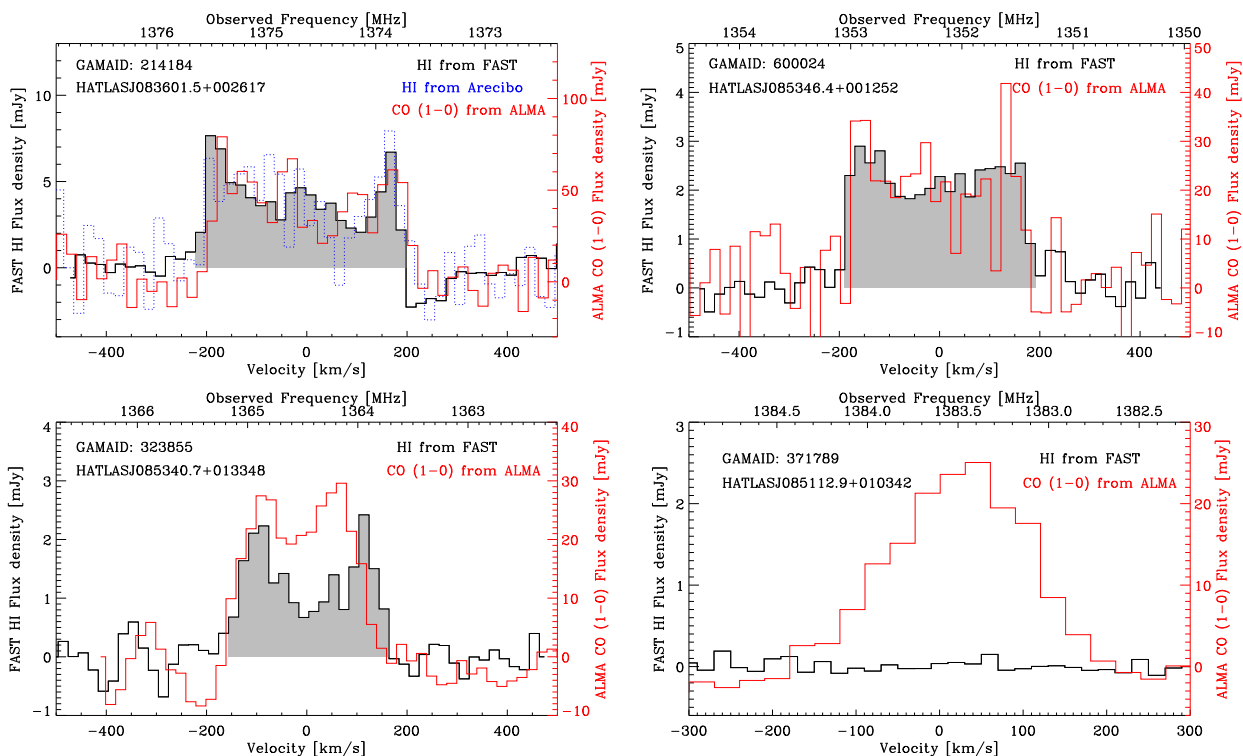


**Fig. 2.** The black thick lines show the HI spectra obtained from FAST. The HI spectra are rebinned into 20 km/s resolution. The red dot lines are the CO (1-0) line from our previous ALMA survey. The scales of the CO emission lines are shown in the right y-axis. We adopt the optical spectroscopy redshift to derive the line velocity. We show the ALFALFA HI spectrum of the galaxy HATLASJ083601.5+002617 in blue color in the upper left panel. Effective on-target integration time of Arecibo telescope is about 48 s. The edges of the emission lines are very sharp, and we obtain a consistency line width with the ALFALFA results. The grey regions highlight the velocity channels we used to derive the HI flux.

(M01). Details for the FAST technical performance can be found in Jiang et al. (2020).

To mitigate the errors due to an unsteady baseline at the GHz frequency, we set the observations as 5 min ON-target + 5 min OFF-target per iteration, and made from 3 to 8 iterations per target. The OFF-target pointing position was chosen at 5.8 arcmin distance, with no sources in the Focus of View (FoV) with a similar redshift (from SDSS spec- $z$  catalogue) as our targets. We use the flux from the OFF pointing to estimate the background, and thus the ON-OFF spectra is the flux from our target.

We calibrate the flux by the noise diode with known antenna temperature that injected into the receiver during the observation (Jiang et al. 2020). Detail data reduction and calibration process are briefly described in Sec. A.

### 3. Results

The noise levels reached for each target are listed in Table 1, while the HI spectra are shown in Fig. 2. For a 5 min on-target integration, we got the noise level about  $2.6 \text{ mJy beam}^{-1}$  at  $1.7 \text{ km s}^{-1}$  velocity resolution bin. The rms declines with the on-target integration time, but not in the manner of  $\propto 1/\sqrt{t}$ , which might be caused by the pointing jitter in the commissioning stage, or weak interference we have not been aware of. We detect the HI emission line in three galaxies. For the HI undetected galaxy, we estimate the flux upper limit as  $5 \times \text{rms} \times 300 W_{300} \text{ mJy km/s}$ , where  $W_{300} = \text{Width}/300 \text{ km/s}$ . All three detected spectra show the double-horn pattern with a typical Full Width Half Maximum (FWHM) of about  $300 \text{ km s}^{-1}$ . We re-sample the HI spectrum into  $\Delta V = 20 \text{ km s}^{-1}$  channels, and derive the integrated HI flux by summing over the velocity channels within Full

Width at Zero Intensity (FWZI), which includes the channels at both line wings with the channel flux higher than the rms. We highlight the velocity channels that used to derive the HI flux in grey color in Fig. 2).

We derive the HI mass following Giovanelli & Haynes (2015):

$$\frac{M_{\text{HI}}}{M_{\odot}} = \frac{2.35 \times 10^5 D_{\text{Mpc}}^2}{1+z} \int_{\text{FWZI}} S(V) dV, \quad (1)$$

where the  $S(V)$  is the flux density in unit of  $\text{Jy beam}^{-1}$ . The uncertainty is estimated by the  $\sigma^2 = (\sqrt{N_{\text{channel}}} \Delta V \times \text{rms})^2 + (10\% \times \text{flux})^2$ , where  $N_{\text{channel}}$  is the number of integration channels, the  $10\% \times \text{flux}$  would account for the uncertainty of the flux calibration. The HI mass or mass upper limit of our targets are listed in Table 2.

### 4. Discussion

#### 4.1. Comparison with a previous ALFALFA result

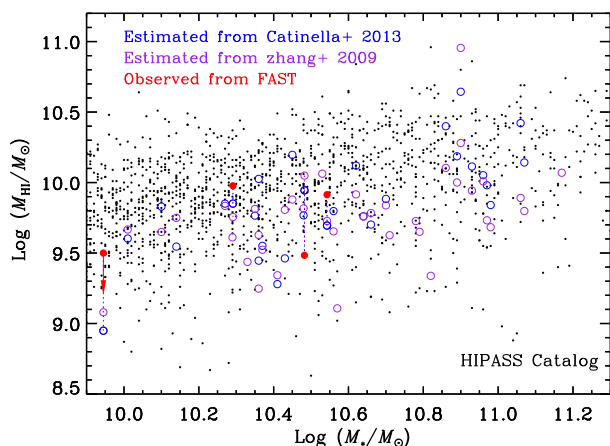
For HATLASJ083601.5+002617, in upper left panel of Fig. 2 we show the results from both FAST and Arecibo telescopes. The ALFALFA survey is in the drift scan mode, and the effective on the target integration time for the ALFALFA spectrum is about 48 s (Haynes et al. 2011). The observed spectra show consistent line profiles. The integrated flux of the Arecibo spectrum given in Haynes et al. (2018) is  $1.68 \pm 0.14 \text{ mJy km s}^{-1}$ , and the FWHM is  $390 \pm 19 \text{ km s}^{-1}$ , both values consistent with our results (see Table 1). This indicates a reasonable flux calibration for the FAST 19-beam receiver in this commissioning phase experiment. In terms of noise levels, at  $20 \text{ km s}^{-1}$ , we

**Table 1.** FAST observation results.  $W_{300}$  = Width/300 km/s is used to estimate the H I flux of HATLASJ085112.9+010342.

HATLAS ID	GAMAID	$t_{\text{int}}$ min	rms @ 1.7 km s <sup>-1</sup> mJy beam <sup>-1</sup>	H I flux mJy km s <sup>-1</sup>	H I FWHM km s <sup>-1</sup>	Peak to peak km s <sup>-1</sup>
HATLASJ083601.5+002617	214184	5	2.61	1696.5 ± 188.1	388±10	361.1
HATLASJ085346.4+001252	600024	10	1.59	812.6 ± 85.2	364±10	328.1
HATLASJ085340.7+013348	323855	15	0.97	410.4 ± 42.3	341±10	229.6
HATLASJ085112.9+010342	371789	20	0.73	< 1095 $W_{300}$		

**Table 2.** Target properties. The lower limit of the log  $M_{\text{bary}}$  is estimated by  $M_{\text{H}_2} + M_*$ 

GAMAID	$z_{\text{spec}}$	log $M_{\text{H I}}$ $M_{\odot}$	log $L'_{\text{CO}}$ K km/s pc <sup>2</sup>	CO FWHM km/s	log $M_*$ $M_{\odot}$	log $M_{\text{dyn}}^{\text{CO}}$ $M_{\odot}$	log $M_{\text{bary}}$ $M_{\odot}$	log $M_{\text{dyn}}^{\text{H I}}$ $M_{\odot}$
214184	0.0332	9.91 ± 0.12	9.02 ± 0.02	391.2	10.59 ± 0.1	10.75±0.02	10.68±0.02	11.96 ± 0.05
600024	0.0504	9.96 ± 0.11	8.88 ± 0.01	349.9	10.31 ± 0.1	10.89±0.05	10.51±0.04	11.90 ± 0.03
323855	0.0410	9.48 ± 0.11	8.79 ± 0.02	342.4	10.36 ± 0.1	10.77±0.08	10.56±0.03	11.30 ± 0.03
371789	0.0266	< 9.53 + log $W_{300}$	8.30 ± 0.07	197.2	10.14 ± 0.1	9.89±0.24	>10.17	


**Fig. 3.** Predicted H I masses of our VALES sample based on the empirical relations in Zhang et al. (2009, in purple circles) and in Catinella et al. (2013, in blue circles). The black dots are the galaxies from HIPASS (Parkash et al. 2018). The red dots show the results of the FAST observation. We link the predicted and the observed H I mass by dot lines. We show the FAST non-detected target by upper limits.

reach 0.8 mJy beam<sup>-1</sup> for 5 min integration time, corresponding to about 2 mJy beam<sup>-1</sup> for 48s integration, while the rms given in ALFALFA H I catalogue is 2.89 mJy beam<sup>-1</sup> at 10 km/s resolution, which is about 2 mJy beam<sup>-1</sup> at 20 km/s resolution. Thus it appears that, in the commissioning phase, the FAST already reached a sensitivity similar to that of ALFALFA.

#### 4.2. The H I gas mass

Previous studies have shown empirical correlations to derive the H I gas mass from the global optical properties such as the color, surface brightness, and the stellar mass densities (e.g., Zhang et al. 2009; Catinella et al. 2013; Parkash et al. 2018) with typical scatters about 0.5 dex. In Fig. 3, we show the observed and estimated H I mass of our VALES sample based on the relations given by Catinella et al. (2013):

$$\log(M_{\text{H I}}/M_*) = -0.338 \log \Sigma_* - 0.235(NUV - r) + 2.908, \quad (2)$$

where  $\Sigma_* = M_*/\pi R_{\text{opt}}^2$  [ $M_{\odot}/\text{kpc}^2$ ] is the stellar mass surface density,  $R_{\text{opt}}$  is the  $r$  band half light radius, and the relation from Zhang et al. (2009):

$$\log(M_{\text{H I}}/M_*) = -1.73238(g - r) + 0.215182\mu_i - 4.08451, \quad (3)$$

where  $\mu_i$  [mag/arcsec<sup>2</sup>] is the SDSS  $i$  band average surface brightness. We adopt the stellar mass, radius and the photometry from GAMA galaxy structure catalogue (Kelvin et al. 2012) and  $H$ -ATLAS catalogue (Valiante et al. 2016). We also show the observed results from H I Parkes All-Sky Survey catalogue (HIPASS, Parkash et al. 2018) in Fig. 3 as a comparison.

In Villanueva et al. (2017) we show that the VALES sample stands for the galaxy population from star-forming (for the  $z \sim 0.05$  galaxies) to the starburst (mainly at  $z > 0.1$ , see the Fig. 1 of Villanueva et al. 2017). We found the VALES sample follow the Kennicutt-Schmidt relation based on the H<sub>2</sub> gas mass from CO( $J = 1 - 0$ ) observations, and the H I gas mass derived from the empirical relation (Zhang et al. 2009). Our pilot survey results show a consistency between estimated and observed H I mass, suggesting that the star-forming galaxies at redshift 0.05 in VALES sample may still follow the Kennicutt-Schmidt relation. More H I observations of the VALES galaxies by FAST are still ongoing.

#### 4.3. Dynamical masses

In Molina et al. (2019), we presented a dynamical analysis to 39 VALES galaxies using the spatial extension of the CO( $J = 1 - 0$ ) emission. For the three H I detected galaxies in this work, the dynamical study shows that the CO rotation curves are still increasing or just about to turn to flat rotation curve with the radius (see the Appendix A of Molina et al. 2019). While comparing the H I and CO( $J = 1 - 0$ ) emission line spectra, we find that the CO( $J = 1 - 0$ ) line profiles in Fig. 2 show a sharp decline at larger velocities, and a similar line width and profile as the H I spectra (see the CO FWHM in Table 2). The agreement of the CO and H I line width suggests that the observed CO( $J = 1 - 0$ ) emission might extend up to the region where the rotation curve is flat (Dickey & Kazes 1992; Sofue 1992; Schoniger & Sofue 1994; de Blok et al. 2016; Tiley et al. 2016).

We can roughly estimate the dynamical mass based on the H I FWHM, and H I radius ( $R_{\text{H I}}$ ) by  $M_{\text{dyn}}^{\text{H I}} = (\text{FWHM}/2/\sin\theta)^2 R_{\text{H I}}/G$ , where  $\theta$  is the H I inclination angle,  $R_{\text{H I}}$  is the H I radius. Since for galaxies the H I size is tightly correlated to the H I mass (Wang et al. 2016; Stevens et al. 2019), the  $R_{\text{H I}}$  can be estimated from  $M_{\text{H I}}$  using the relation derived by Wang et al. (2016). For the H I mass range of  $9.5 < \log(M_{\text{H I}}/M_{\odot}) < 10$ , the H I radius is in the range of 16.5 to 30 kpc (See Eqn. 2 or Fig. 1 in Wang et al. 2016), which is much larger than the CO radius (see the red contours in Fig. B.1). We do not have inclination information of the H I gas.

But if we assume the Ks band image and H<sub>I</sub> have a similar inclination angle (Molina et al. 2019), we can roughly estimate the  $M_{\text{dyn}}^{\text{H}_I}$  (see Table 2). The  $M_{\text{dyn}}^{\text{H}_I}$  is about one order of magnitude larger than the baryon mass ( $M_{\text{bary}} = M_{\text{H}_I} + M_{\text{H}_2} + M_*$ , also listed in Table 2. For HATLASJ085112.9+010342, which has no H<sub>I</sub> detection, we estimate the lower limit of the baryon mass as  $M_{\text{bary}}^{\text{lower limit}} = M_{\text{H}_2} + M_*$ ). The H<sub>I</sub> radii of our targets are much larger than the optical and CO radii, yielding a larger  $M_{\text{dyn}}^{\text{H}_I}$ . The larger  $M_{\text{dyn}}^{\text{H}_I}$  may suggest that H<sub>I</sub> mainly traces the dynamical mass within a larger radius where the dark matter start to dominate the gravitational potential.

On the other hand, our previous work also derived the dynamical mass within  $2 \times r_{1/2\text{CO}}$  from CO velocity map (Molina et al. 2019), where the half light CO radius ( $r_{1/2\text{CO}}$ ) is about 4 kpc. We list the  $M_{\text{dyn}}^{\text{CO}}$  in Table 2 and we can see a good consistency between the  $M_{\text{dyn}}^{\text{CO}}$  and the baryon mass. Considering the higher dynamical masses derived from the H<sub>I</sub> data, this implies that CO dynamics is restricted, as expected, to the gravitational potential of the central regions in galaxies. Therefore, it might be possible to trace dark matter halos using both CO and H<sub>I</sub> observations. We show the optical image, CO contours as well as the H<sub>I</sub> spectra of our targets in Sec. B. The target HATLASJ085340.7+013348 has a clumpy CO morphology, which might be the reason of the relatively higher CO to H<sub>I</sub> flux ratio in Fig. 2.

## 5. Conclusion

We report on some of the first extragalactic H<sub>I</sub> line observations made during the commissioning phase of the FAST 19-beam receiver, of four star-forming galaxies at  $z \approx 0.05$  taken from the VALES survey. These are among the first extragalactic H<sub>I</sub> detection results during the FAST commissioning phase stage. Using 5min/5min ON/OFF pointing observations, we reached an rms of  $2.6 \text{ mJy beam}^{-1}$  at a spectral resolution  $1.7 \text{ km s}^{-1}$ . We detected three out of the four observed galaxies. One of our targets was detected previously by the Arecibo ALFALFA survey, with results consistent with ours. The observed H<sub>I</sub> masses are consistent with values estimated using previously determined empirical relations (Zhang et al. 2009; Catinella et al. 2013), with a scatter of about 0.5 dex. We find the width of the H<sub>I</sub> emission is similar to the CO( $J = 1 - 0$ ) width revealed by ALMA, suggesting that ALMA observations already observed the flat rotation curve from the galaxy outskirts. The dynamical mass that estimated from H<sub>I</sub> ( $M_{\text{dyn}}^{\text{H}_I}$ ) is an order of magnitude higher than the baryon mass ( $M_* + M_{\text{H}_2} + M_{\text{H}_I}$ ) and the dynamical masses derived from CO observations ( $M_{\text{dyn}}^{\text{CO}}$ ), implying that the dynamical mass traced by H<sub>I</sub> would be more dominated by dark matter halo.

*Acknowledgements.* We thank the referee for carefully reading and for patiently providing constructive comments that helped us to improve the quality of this paper. C.C. appreciates the kindness help from FAST, especially to Lei Qian, Ningyu Tang, Jing Tang and Zheng Zheng, and helpful discussions about FAST observation configuration and data reduction with Pei Zuo, Niankun Yu and Lizhi Xie. This work made use of the data from FAST (Five-hundred-meter Aperture Spherical radio Telescope). FAST is a Chinese national mega-science facility, operated by National Astronomical Observatories, Chinese Academy of Sciences. C.C. is supported by the National Natural Science Foundation of China (NSFC), No. 11803044, 11673028. J.H. is supported by NSFC, No. 11933003. This work is sponsored (in part) by the Chinese Academy of Sciences (CAS), through a grant to the CAS South America Center for Astronomy (CASSACA). E.I. acknowledges partial support from FONDECYT through grant N° 1171710. D.W. is supported by NSFC, No. U1931109, 11733006. T.M.H. acknowledges the support from the Chinese Academy of Sciences (CAS) and the National Commission for Scientific and Technological Research of Chile (CONICYT)

through a CAS-CONICYT Joint Postdoctoral Fellowship administered by the CAS South America Center for Astronomy (CASSACA) in Santiago, Chile. This work was supported by the National Science Foundation of China (11721303, 11991052) and the National Key R&D Program of China (2016YFA0400702). CKX acknowledges support from the National Key R&D Program of China No. 2017YFA0402704 and National Natural Science Foundation of China No. 11873055 and No. 11733006. This paper makes use of the following ALMA data: ADS/JAO.ALMA#2013.1.00530.S. ALMA is a partnership of ESO (representing its member states), NSF (USA) and NINS (Japan), together with NRC (Canada), MOST and ASIAA (Taiwan), and KASI (Republic of Korea), in cooperation with the Republic of Chile. The Joint ALMA Observatory is operated by ESO, AUI/NRAO and NAOJ. In addition, publications from NA authors must include the standard NRAO acknowledgement: The National Radio Astronomy Observatory is a facility of the National Science Foundation operated under cooperative agreement by Associated Universities, Inc.

## References

- Aihara, H., AlSaiyad, Y., Ando, M., et al. 2019, PASJ, 71, 114  
 Barnes, D. G., Staveley-Smith, L., de Blok, W. J. G., et al. 2001, MNRAS, 322, 486  
 Bournaud, F., Combes, F., Jog, C. J., & Puerari, I. 2005, A&A, 438, 507  
 Catinella, B., Schiminovich, D., Cortese, L., et al. 2013, MNRAS, 436, 34  
 Cheng, C., Ibar, E., Hughes, T. M., et al. 2018, MNRAS, 475, 248  
 de Blok, W. J. G., Walter, F., Smith, J. D. T., et al. 2016, AJ, 152, 51  
 Deg, N., Blyth, S. L., Hank, N., Kruger, S., & Carignan, C. 2020, MNRAS, 495, 1984  
 Dickey, J. M. & Kazes, I. 1992, ApJ, 393, 530  
 Driver, S. P., Norberg, P., Baldry, I. K., et al. 2009, Astronomy and Geophysics, 50, 5.12  
 Eales, S., Dunne, L., Clements, D., et al. 2010, PASP, 122, 499  
 Fernández, X., Gim, H. B., van Gorkom, J. H., et al. 2016, ApJ, 824, L1  
 Giovanelli, R. & Haynes, M. P. 2015, A&A Rev., 24, 1  
 Giovanelli, R., Haynes, M. P., Kent, B. R., et al. 2005, AJ, 130, 2598  
 Haynes, M. P., Giovanelli, R., Kent, B. R., et al. 2018, ApJ, 861, 49  
 Haynes, M. P., Giovanelli, R., Martin, A. M., et al. 2011, AJ, 142, 170  
 Hu, W., Wang, X., Wu, F., et al. 2020, MNRAS, 493, 5854  
 Huang, S., Haynes, M. P., Giovanelli, R., & Brinchmann, J. 2012, ApJ, 756, 113  
 Jaffé, Y. L., Poggianti, B. M., Verheijen, M. A. W., Deshev, B. Z., & van Gorkom, J. H. 2013, MNRAS, 431, 2111  
 Jiang, P., Tang, N.-Y., Hou, L.-G., et al. 2020, arXiv e-prints, arXiv:2002.01786  
 Jiang, P., Yue, Y., Gan, H., et al. 2019, Science China Physics, Mechanics, and Astronomy, 62, 959502  
 Kelvin, L. S., Driver, S. P., Robotham, A. S. G., et al. 2012, MNRAS, 421, 1007  
 Kennicutt, Robert C., J. 1998, ARA&A, 36, 189  
 Kerp, J., Winkel, B., Ben Bekhti, N., Flöer, L., & Kalberla, P. M. W. 2011, Astronomische Nachrichten, 332, 637  
 Koribalski, B. S., Staveley-Smith, L., Westmeier, T., et al. 2020, arXiv e-prints, arXiv:2002.07311  
 Lang, R. H., Boyce, P. J., Kilborn, V. A., et al. 2003, MNRAS, 342, 738  
 Leroy, A. K., Walter, F., Brinks, E., et al. 2008, AJ, 136, 2782  
 Maddox, N., Hess, K. M., Obreschkow, D., Jarvis, M. J., & Blyth, S. L. 2015, MNRAS, 447, 1610  
 Meyer, M. 2009, in Panoramic Radio Astronomy: Wide-field 1-2 GHz Research on Galaxy Evolution, 15  
 Meyer, M. J., Zwaan, M. A., Webster, R. L., et al. 2004, MNRAS, 350, 1195  
 Molina, J., Ibar, E., Villanueva, V., et al. 2019, MNRAS, 482, 1499  
 Nan, R. 2006, Science in China: Physics, Mechanics and Astronomy, 49, 129  
 Nan, R., Li, D., Jin, C., et al. 2011, International Journal of Modern Physics D, 20, 989  
 Neelaman, M., Prochaska, J. X., Ribaud, J., et al. 2016, ApJ, 818, 113  
 Oke, J. B. & Gunn, J. E. 1983, ApJ, 266, 713  
 Parkash, V., Brown, M. J. I., Jarrett, T. H., & Bonne, N. J. 2018, ApJ, 864, 40  
 Qiu, Y. H. 1998, MNRAS, 301, 827  
 Rhee, J., Lah, P., Briggs, F. H., et al. 2018, MNRAS, 473, 1879  
 Roberts, M. S. 1978, AJ, 83, 1026  
 Salucci, P. 2019, A&A Rev., 27, 2  
 Schmidt, M. 1959, ApJ, 129, 243  
 Schoniger, F. & Sofue, Y. 1994, A&A, 283, 21  
 Sofue, Y. 1992, PASJ, 44, L231  
 Stevens, A. R. H., Diemer, B., Lagos, C. d. P., et al. 2019, MNRAS, 490, 96  
 Tiley, A. L., Bureau, M., Saintonge, A., et al. 2016, MNRAS, 461, 3494  
 Valiante, E., Smith, M. W. L., Eales, S., et al. 2016, MNRAS, 462, 3146  
 Villanueva, V., Ibar, E., Hughes, T. M., et al. 2017, MNRAS, 470, 3775  
 Wang, J., Koribalski, B. S., Serra, P., et al. 2016, MNRAS, 460, 2143  
 Winkel, B., Kalberla, P. M. W., Kerp, J., & Flöer, L. 2010, ApJS, 188, 488  
 Wong, O. I., Ryan-Weber, E. V., Garcia-Appadoo, D. A., et al. 2006, MNRAS, 371, 1855  
 Yun, M. S., Ho, P. T. P., & Lo, K. Y. 1994, Nature, 372, 530  
 Zhang, K., Wu, J., Li, D., et al. 2019, Science China Physics, Mechanics, and Astronomy, 62, 959506  
 Zhang, W., Li, C., Kauffmann, G., et al. 2009, MNRAS, 397, 1243

## Appendix A: Data reduction and flux calibration

Fig. A.1 shows the data reduction flowchart. The data is reduced in chunks of 10 min. Each chunk includes 300 spectra for the ON target and 300 spectra red for the OFF target (background). If the redshifted H $\alpha$  line suffers from temporal RFI, we simply ignore these 10 min data. The left two panels in Fig. A.1 are the spectra we obtained in the 5 min ON (upper panel) and 5 min OFF the target (bottom panel).

A noise diode is used for FAST signal calibration (Jiang et al. 2020). When it is ‘on’, it injects a noise of known temperature to the receiver. The noise diode is switched between ‘on’ and ‘off’ repeatedly during the whole FAST observation. Noise ‘on’ and ‘off’ are in the periods twice the signal sampling period. We extract one spectrum per 1.006632926s. Half of the spectra contains noise with known temperature from noise diode. For a given target, comparing the spectra with noise diode ‘on’ and ‘off’, we can derive the intensity (i.e. antenna temperature) of these spectra (Jiang et al. 2020).

Our spectra can be classified in four classes, ON target with noise diode ‘on’ and ‘off’ ( $f_{\text{ON}}^{\text{cal on}}$  and  $f_{\text{ON}}^{\text{cal off}}$ ), and OFF target with noise diode ‘on’ or ‘off’ ( $f_{\text{OFF}}^{\text{cal on}}$  and  $f_{\text{OFF}}^{\text{cal off}}$ ). These four classes are shown in the middle-left panels of Fig. A.1. Note these have not been yet calibrated in flux density.

The flux calibration is done via the following two formulas:  $T_{\text{ON}}^{\text{cal off}}/f_{\text{ON}}^{\text{cal off}} = T_{\text{noise}}/(f_{\text{ON}}^{\text{cal on}} - f_{\text{ON}}^{\text{cal off}})$ , and  $(T_{\text{ON}}^{\text{cal on}} + T_{\text{noise}})/f_{\text{ON}}^{\text{cal on}} = T_{\text{noise}}/(f_{\text{ON}}^{\text{cal on}} - f_{\text{ON}}^{\text{cal off}})$ , where  $T_{\text{noise}}$  is the known noise temperature in Kelvin, the  $T_{\text{ON}}^{\text{cal on}}$  and  $T_{\text{ON}}^{\text{cal off}}$  are the calibrated antenna temperatures of the signal data, with noise diode ‘on’ and ‘off’ (see the Sec. 3.1 of Jiang et al. 2020). The average calibrated spectra of four classes are shown in the middle right panels of Fig. A.1. These are inverse-variance weighted means of individual spectra, and the rms error is estimated as  $\sigma \propto T_{\text{sys}}/\sqrt{\Delta V t}$ , where the system temperature  $T_{\text{sys}} \sim 20$  K, the channel width  $\Delta V = 1.7$  km s $^{-1}$ , and the  $t$  here is the integration time. The right panel of Fig. A.1 shows the weighted average spectra temperature ( $T_a$ ) of the ON and OFF targets in the units of Kelvin.

We find a clear increment of the noise as we move to higher frequencies, starting at  $\sim 1373.5$  MHz to 1374.5 MHz (see white boxes in Fig. A.1), indicating an unstable background noise. In order to assess this quantitatively, we derive additional mean spectra for the OFF position in two time intervals: the first 0~74 s and the second 75~147 s separately. We compare the mean OFF spectra of different time intervals and find that the background temperature increases by  $\sim 0.1$  K during the 5 min integration, with a larger increase about 0.3 K at 1373.5 MHz (purple and green color curves in the middle right panel of Fig. A.1). In the right panel of Fig. A.1, we can also see that the target OFF spectrum (blue line) is about 0.15 K higher than the target ON spectrum (red).

We adopt a 14.86 K Jy $^{-1}$  conversion factor, which has an accuracy of the order of 10% (Jiang et al. 2020).

We subtract the baseline using model-fit based on a sinusoidal plus a linear function, where the sine function would account for the standing wave, and the linear function would represent the trend of the baseline between 1372 MHz and 1376 MHz. As an example, the final steps of the data reduction of a target are illustrated in Fig. A.2. The generation of the final spectrum can be seen in the left panel of Fig. A.2. The minus temperature is caused by the increasing background noise. We correct the Doppler velocity and convert the spectrum velocity into kinematical Local Standard of Rest, and show the final spectrum in the right panel of Fig. A.2.

Each FAST spectrum includes the spectra with two polarizations individually. Since H $\alpha$  emission from galaxies should not be polarized, we inspected both polarizations separately to check if the rms or detections are consistent. The right panel of Fig. A.2 shows the two polarizations in blue and red colours. We do not find significant differences in polarisation, so we simply combined the spectra of both polarizations together during the data reduction.

## Appendix B: Fake color image of our targets

We show the CO contour and the optical images of our targets in Fig. B.1. we can see that the CO morphology is compact in the galaxy center for HATLASJ085346.4+001252, HATLASJ083601.5+002617, and HATLASJ085112.9+010342. And for the galaxy HATLASJ085340.7+013348, the CO morphology is clumpy. We also see that the H $_2$  to H $\alpha$  flux ratio for HATLASJ085340.7+013348 is about 15, while the rest two targets have CO to H $\alpha$  flux ratios about 10. This might suggest a more efficient formation of H $_2$  molecules in a nuclear region, and a possible connection between CO morphology and the CO to H $\alpha$  flux ratio.

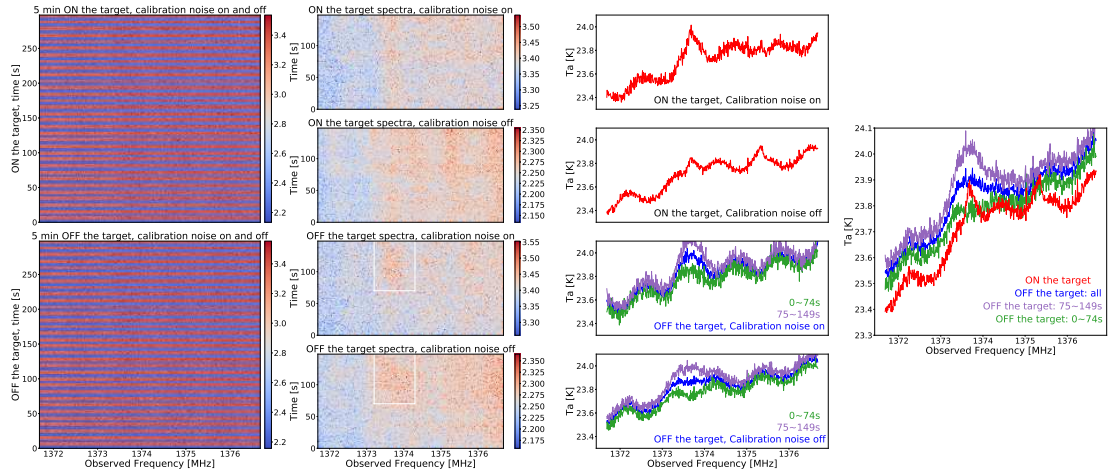


**Fig. A.1.** Data reduction pipeline: **Left two panels:** Each panel shows the raw spectra for the 5-min ON- or OFF-target positions (upper and lower panel respectively). The x-axis is the observed frequency, the y-axis shows the sampling time of the spectra, with a sampling rate of once every 1.006632926s (0.993411 Hz). The signal intensity in individual spectra (300 of them in each panel) is represented by colors, with the scale illustrated by the color bar on the right side of each panel. Note that those spectra in “red stripes” were sampled when calibration noise was on, and those in “blue stripes” were sampled when the calibration noise was off (see text). Unit of the color bar is digital number /  $10^{12}$  from ADU, which needs to be calibrated into temperature unit. **Middle left panels:** We split the raw spectra into four cases: ON/OFF the target with calibration noise on/off. **Middle right panel:** The average spectra of the four classes. We show the total background in blue color, and the background from the first and rest 74 seconds (green and purple color) in the lower two panels. The green line show a lower temperature than the purple line, implying a increasing system temperature. **Right panel:** Spectra of the ON and OFF the target.

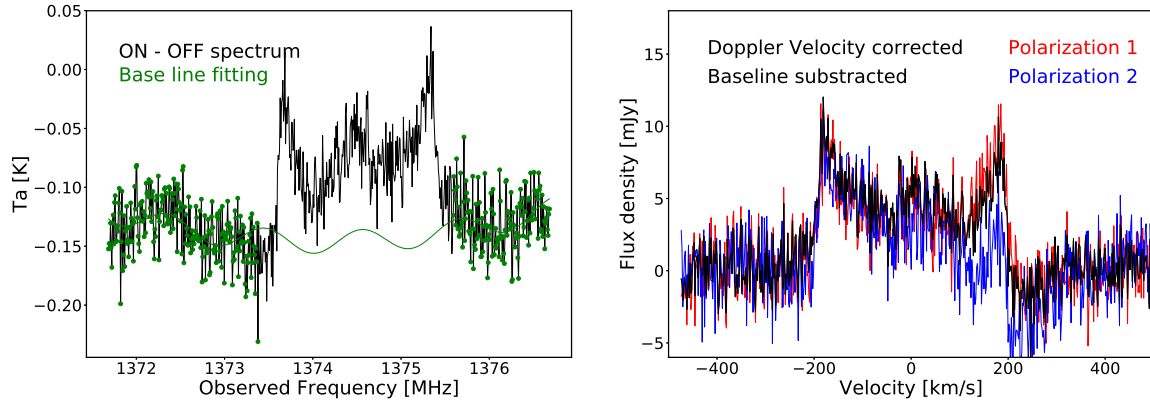


**Fig. A.2.** Flux calibration: **left panel:** We fit the baseline from the data shown in green dots with the function  $A * \sin(kx + b) + mx + n$  to account for the stand wave. **right panel:** We correct the Doppler velocity and convert the antenna temperatures to flux intensities in mJy. HI emission from galaxies should have no polarization. As a consistency check, we also reduce the spectrum including only one polarization, and show the results in blue and red colors.

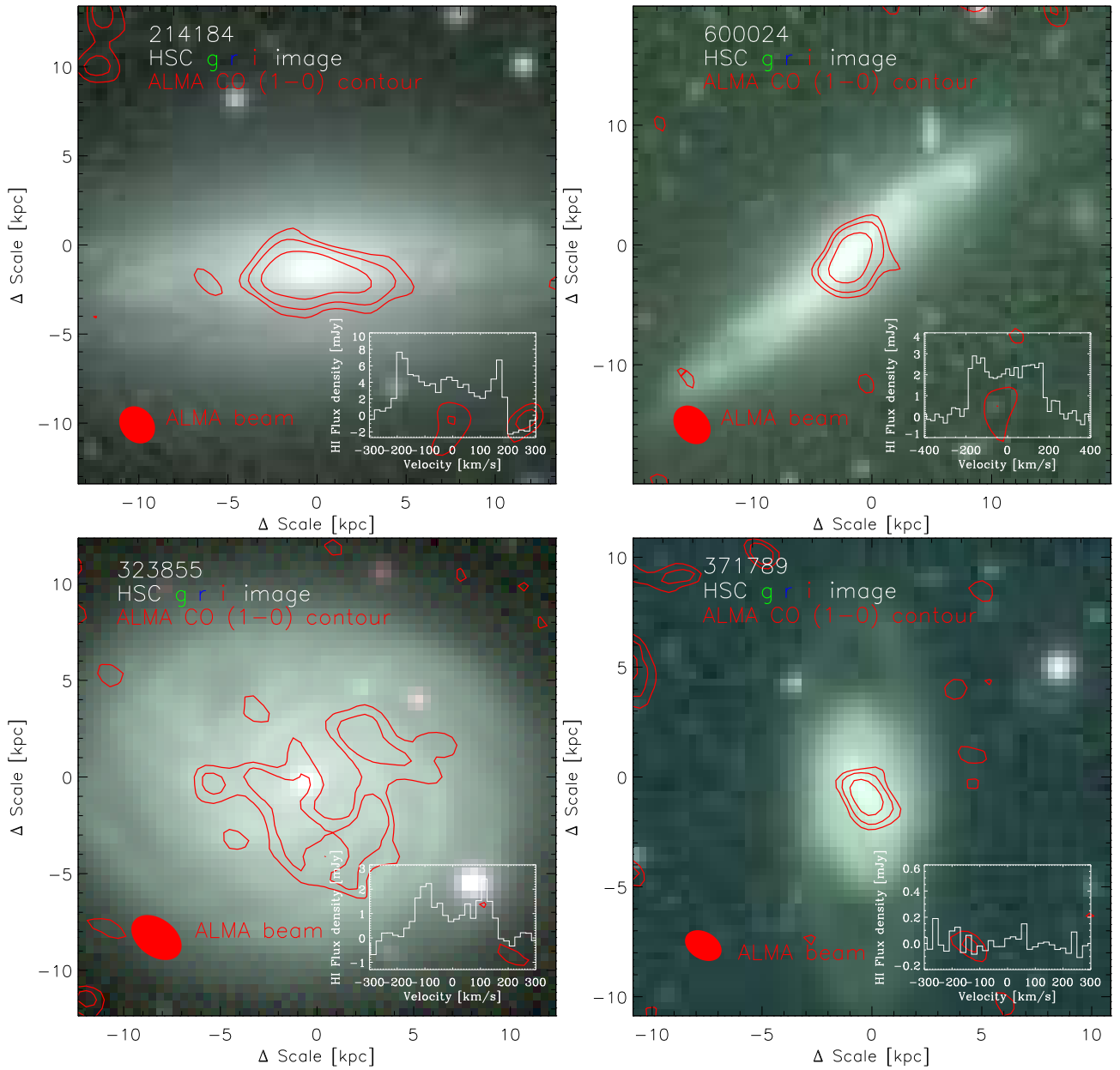


**Fig. B.1.** Color images composed g, r, i band images from the HSC survey wide fields (Aihara et al. 2019), as well as the red contour of ALMA CO (1-0) moment 0 map. The contours are shown in  $[2, 3, 5] \times$  rms. We also show the HI spectrum in 20 km/s velocity bin at the lower right corner of each panel. The FAST beam size (2.9 arcmin) is corresponding to about 130 kpc at redshift 0.05, much larger than the scale of the images.